

1                   **A simple predictive model for the eddy propagation**  
2                   **trajectory in the northern South China Sea**

3  
4                   Jiaxun Li<sup>1,2</sup>, Guihua Wang<sup>\*1</sup>, Huijie Xue<sup>3,4</sup>, and Huizan Wang<sup>5</sup>

5  
6                   <sup>1</sup>Department of Atmospheric and Oceanic Sciences, Institute of Atmospheric Science,  
7 Fudan University, Shanghai, China

8                   <sup>2</sup>Naval Institute of Hydrographic Surveying and Charting, Tianjin, China

9                   <sup>3</sup>State Key Laboratory of Tropical Oceanography, South China Sea Institute of  
10 Oceanology, Chinese Academy of Sciences, Guangzhou, China

11                   <sup>4</sup>School of Marine Sciences, University of Maine, Orono, Maine, USA

12                   <sup>5</sup>Institute of Meteorology and Oceanography, National University of Defense  
13 Technology, Nanjing, China

14  
15                   Corresponding author: Guihua Wang, Department of Atmospheric and Oceanic  
16 Sciences, Institute of Atmospheric Science, Fudan University, Shanghai, China.  
17 (wghocean@yahoo.com)

19 **Abstract** A novel predictive model is built for eddy propagation trajectory using the  
20 multiple linear regression method. This simple model has related various oceanic  
21 parameters to eddy propagation position changes in the northern South China Sea  
22 (NSCS). These oceanic parameters mainly represent the effects of  $\beta$  and mean flow  
23 advection on the eddy propagation. The performance of the proposed model is  
24 examined in the NSCS based on five years of satellite altimeter data, and  
25 demonstrates its significant forecast skills over a 4-week forecast window comparing  
26 to the traditional persistence method. It is also found that the model forecast accuracy  
27 is sensitive to eddy polarity and forecast season.

28

## 29 **1. Introduction**

30 Mesoscale eddies are coherent rotating structures that are ubiquitous over most of the  
31 world's oceans (Chelton et al., 2007). They play an important role in the transport of  
32 momentum, heat, mass and chemical and biological tracers, thereby become critical  
33 for issues such as general circulation, water mass distribution, ocean biology and  
34 climate change (Wang et al., 2012; Dong et al., 2014; Zhang et al., 2014; Ma et al.,  
35 2016; Li et al., 2017). Therefore, forecasting the eddy propagation positions  
36 accurately is not only important scientifically but also important practically for  
37 problems such as ocean observing systems designing, fishing planning, and  
38 underwater acoustic detecting.

39

40 Traditionally, ocean dynamical models were used as the tool of predicting the  
41 evolution of ocean eddies (Robinson et al., 1984). Since mesoscale eddies are often  
42 associated with strong nonlinear processes and their dynamical mechanisms are quite  
43 different, the operational forecast of eddies has been a big challenge to ocean  
44 numerical model. Much progress has been made in recent years in eddy-resolving  
45 ocean prediction. With the data assimilation and the increasing of model resolution,  
46 the model increases forecast skill. Daily forecast errors of eddy center positions in the  
47 northwestern Arabian Sea and Gulf of Oman are 44-68 km in 1/12° global HYCOM  
48 model, and reach to 22.5-37 km in 1/32° NLOM model (Hurlburt et al., 2008). The  
49 forecast skill and predictability of dynamical models can only be increased by better  
50 assimilation schemes (initialization), sufficient data (especially the subsurface), and  
51 improving resolution (physics and computing) (Rienecker et al., 1987; Oey et al.,  
52 2005). These restrictions preclude the all-pervading operational use of dynamical  
53 models when these initial data and computing power are not feasible due to some  
54 reasons.

55

56 In this paper, we developed a simple statistical model to predict the eddy positions 1-4  
57 weeks in advance using only the past positions of the eddy and its surrounding fields.

58 Our “test block” of ocean is the northern South China Sea (NSCS). South China Sea  
59 is a semi-enclosed sea under the dramatic influence of the East Asian Monsoon and  
60 Kuroshio intrusion (Liu and Xie, 1999; Shaw, 1991). Due to the variable external  
61 forcing and complex topography, mesoscale eddies show obvious geographic  
62 distributions and various characteristics (Wang et al., 2003; Xiu et al., 2010; Chen et  
63 al., 2011), but the common character is the overall westward tendency of eddy  
64 trajectories no matter of the eddy polarity (Fig. 1). We will first analyze the pattern  
65 and dynamics of the common westward movement of eddies in the NSCS, then  
66 choose the potential predictors and develop a simple predictive model for eddy  
67 propagation trajectories, and finally evaluate the model performance and discuss the  
68 impact of eddy polarity and season on the forecast accuracy.

## 69 **2. Data and Methods**

### 70 **2.1 Data**

71 The sea level anomalies (SLA) are from the Archiving, Validation and Interpretation  
72 of Satellite Oceanographic data (AVISO, <ftp://ftp.aviso.oceanobs.com/>) (Ducet et al.,  
73 2000). The product merges the measurements of TOPEX/Poseidon, European Remote  
74 Sensing Satellite (ERS-1/2), Geosat Follow-on, Jason-1/2, and Envisat, and spans the  
75 period from October 14, 1992 to August 7, 2013. Its temporal resolution is weekly,  
76 and its spatial resolution is  $0.25^\circ$  latitude by  $0.25^\circ$  longitude. To estimate the  
77 large-scale geostrophic currents, we use the absolute dynamic topography (ADT),  
78 which consists of the SLAs and a mean dynamic topography (MDT). The method for  
79 calculating the MDT was introduced by Rio and Hernandez (2004), and the data is  
80 also distributed by AVISO.

81

82 The monthly climatology of observed ocean temperature and salinity from U.S. Navy  
83 Generalized Digital Environment Model (GDEM-Version 3.0) is used to calculate the  
84 phase speed of nondispersive baroclinic Rossby waves in the NSCS. It has a  
85 horizontal resolution of  $0.25^\circ$  latitude by  $0.25^\circ$  longitude, and 78 standard depths from

86 0 to 6600 m with the vertical resolution varying from 2 m at the surface to 200 m  
87 below 1600 m (Canes, 2009).

88

89 The NSCS eddy trajectory data is derived from the 3<sup>rd</sup> release of the global eddy  
90 dataset (<http://cioss.coas.oregonstate.edu/eddies/>). The eddy center positions within  
91 their trajectories are recorded at 7-day time intervals. A detailed description of the  
92 eddy trajectory dataset can be found in Chelton et al. (2011). To forecast the eddy  
93 trajectory 1-4 weeks in advance using the last position of the eddy, only eddies with a  
94 lifetime of 5 weeks or longer are retained in this study.

## 95 **2.2 The Maximum Cross-Correlation Method**

96 The maximum cross-correlation (MCC) method is a space-time lagged technique,  
97 which can estimate the surface motions from time-sequential remote sensing images.  
98 It has been successfully used to track clouds from geosynchronous satellite data  
99 (Leese et al., 1971), to compute sea-ice motion (Ninnis et al., 1986) and advective  
100 surface velocities (Emery et al., 1986) from sequential infrared satellite images, and to  
101 determine the propagation velocities of ocean eddies from satellite altimeter data (Fu,  
102 2006, 2009). The MCC method used in this study is the same as that of Fu (2009),  
103 which is a little different with that of Emery et al. (1986). In the method of Emery et  
104 al., the correlations of the image in the subwindow with all the neighboring ones in  
105 the whole window at the next time are computed, and the speed and direction of the  
106 maximum correlation can be estimated. While in the method of Fu (2009), the  
107 correlations of the SLA at a given location with all the neighboring SLA at various  
108 time lags are computed, and the speed and direction of the maximum correlation can  
109 be estimated. The reason of their difference may be due to the low time-space  
110 resolution of SLA comparing with other infrared satellite images.

111

112 The MCC method mainly consists of two procedures (Fu, 2009): first, the  
113 cross-correlations of the SLA time series ( $h$ ) with others within a certain range box  
114 are computed for some time lags ( $\Delta T$ ) in multiples of 7 days (time resolution of SLA

115 data) at each grid node location  $(x, y)$  as:

$$116 \quad C_{x,y}(\Delta x, \Delta y, \Delta T) = \overline{h(x, y, t)h(x + \Delta x, y + \Delta y, t + \Delta T)} \quad (1)$$

117 where  $\Delta x$  and  $\Delta y$  are the spatial lags and the over bar means time averaging.

118 Second, the position of the maximum correlation at each time lag ( $\Delta T$ ) is identified

119 and a speed can be derived from the time lag and the distance of this position from the

120 origin. Then an average speed vector  $(u, v)$  weighted by the correlation coefficients is

121 calculated from the estimates at various time lags as:

$$122 \quad (u, v) = \frac{\sum_i (\Delta x_i / \Delta T_i, \Delta y_i / \Delta T_i) C_i}{\sum_i C_i} \quad (2)$$

123 where  $C_i$  is the maximum correlation at  $\Delta T_i$ , and  $\Delta x_i, \Delta y_i$  are the distances

124 between the position of maximum correlation and the origin. The average velocities

125 are then assigned to the eddy movement velocities at the given grid point.

126

127 To focus on the global mesoscale eddy, the time lags were limited to less than 70 days

128 and the dimension of the window was less than 400 km (Fu, 2009). While in the

129 NSCS, the time lags should be limited to less than 42 days, since many correlation

130 coefficients are below the 95% confidence level at larger time lags (Zhuang et al.,

131 2010). Besides, Chen et al. (2011) found that eddies propagate with 5.0-9.0 cm/s in

132 the NSCS. Thus the search radius can be generally limited as 300 km (9.0 cm/s\*42

133 days  $\approx$  300 km) to reduce incidence of spurious MCC vectors. Since the mean flow

134 and associated eddy propagation in the SCS have seasonal variability, we divided the

135 weekly SLA data from 1992 to 2013 into four groups according to four seasons

136 (winter: December-February, spring: March-May, summer: June-August, autumn:

137 September-November). Then the seasonal climatological eddy propagation velocities

138 can be estimated from the same seasonal group at intervals of 1 week using the MCC

139 method.

### 140 **2.3 The Multiple Linear Regression Model**

141 To develop a simple statistical predictive model for relating various oceanic

142 parameters to eddy propagation position changes, the multiple linear regression

143 method is used for developing such statistical forecast model. The multiple linear

144 regression is a linear approach to modeling the relationship between the response and  
 145 explanatory variables. This classical method has many practical uses in oceanography  
 146 and meteorology, such as the prediction of Arctic sea ice extent (Zhang, 2015), the  
 147 estimation of subsurface salinity profile (Bao et al, 2019), the estimation of  
 148 anthropogenic CO<sub>2</sub> accumulation in the Southern Ocean (Matear and McNeil, 2003),  
 149 the forecast of typhoon track (Aberson and Sampson, 2003) and intensity (Demaria  
 150 and Kaplan, 1994), Madden-Julian Oscillation forecast (Seo, 2008), and ENSO  
 151 prediction (Dominiak and Terray, 2005).

152

153 In this study, the predictands (dependent variables) are the zonal and meridional  
 154 displacements at each forecast time from the initial position (Table 1). The choice of  
 155 the predictors based on physical analysis will be shown in detail in Section 3. Since  
 156 the variables used for the regression involve different scales and units, it is  
 157 inappropriate to use them directly, as it may cause the fitting to deviate from the  
 158 physical constraints. Thus all the variables are normalized with their anomalies  
 159 divided by their corresponding standard deviations before the regressing. After that,  
 160 the normalized predicted zonal (meridional) displacement  $DX$  ( $DY$ ) can be estimated  
 161 using a multiple linear regression method:

$$162 \quad DX_j = \sum_{i=1}^n a_{i,j} P_i, \quad j = 1, 4 \quad (3)$$

$$163 \quad DY_j = \sum_{i=1}^n b_{i,j} P_i, \quad j = 1, 4 \quad (4)$$

164 where the subscript  $j$  refers to the forecast interval (1-4 weeks), the subscript  $i$  refers  
 165 to the serial number of normalized predictors ( $P$ ),  $n$  represents the number of selected  
 166 predictors;  $a$  and  $b$  donate the regression coefficients of predictors onto  $DX$  and  $DY$ ,  
 167 respectively.

168

169 There are a total of 8 regression equations, i.e., both the meridional and zonal  
 170 directions for the weeks of 1-4. We separate the whole eddy trajectories into two sets:  
 171 one for regressing and the other for forecasting. At week-1, we used 1981 (76%) eddy

172 trajectory segments (a segment is the distance between two neighboring eddy center  
173 positions at 7-day interval on a single eddy trajectory) of 283 eddy trajectories during  
174 1992-2008 for regressing, and 623 (24%) eddy trajectory segments of 81 eddy  
175 trajectories during 2009-2013 for forecasting. The other forecast experiments for 2, 3,  
176 and 4 weeks maintain the same periods for regressing and forecasting. To evaluate the  
177 overall forecast ability of the model, the mean forecast error is defined as the  
178 averaged distance (D) between the predicted eddy positions and the satellite observed  
179 eddy positions following great circle distance (Ali et al., 2007):

$$180 \quad D = R \cdot \arccos[\sin Y_o \sin Y_F + \cos Y_o \cos Y_F \cos(X_o - X_F)] \quad (5)$$

181 where R is the earth radius,  $X_o$  ( $X_F$ ) and  $Y_o$  ( $Y_F$ ) represent the observed (predicted)  
182 longitude and latitude in degrees, respectively.

### 183 **3. Dynamics of Eddy Propagation in the NSCS and Choice of** 184 **Predictors**

#### 185 **3.1 Pattern and Dynamical Analysis of Eddy Propagation in the** 186 **NSCS**

187 One of the most important steps in the development of a regression model is the  
188 choice of independent variables (predictors). In choosing the potential predictors, the  
189 candidates should have a physical link (direct or indirect) with the eddy propagation.  
190 To investigate the dynamical factors associated with eddy propagation in the NSCS,  
191 the pattern of eddy propagation speeds should be estimated firstly.

192

193 Instead of a Lagrangian description of the movement of individual eddies as reported  
194 in the previous studies (e.g., Wang et al., 2003; Chen et al., 2011), the space-time  
195 lagged MCC method provides an Eulerian description of the pattern of eddy  
196 propagation speeds (Fu, 2009). As shown in Fig. 2a and 2d, the MCC method has  
197 mapped the propagation speeds of eddies in the NSCS for the winter and summer  
198 season, respectively. The propagation of eddies is generally westward in the ocean



199 interior and southward in the western boundary with the typical speed of 4-10 cm/s.  
200 The propagation direction of eddies generated southwest of Taiwan is southwestward  
201 along the 200-2000 m isobaths, indicating the steering effects of the ocean's  
202 bathymetry. There are two distinct differences between the winter season and the  
203 summer season: one is that the eddy propagation speed in winter is relatively larger  
204 than that in summer; and the other is that the influence of the western boundary  
205 current can be clearly seen near 16°N-18°N along the Vietnam coast in winter,  
206 creating an organized band of southward eddy propagation pattern, while this cannot  
207 be found in summer. The different patterns of the eddy propagation speed in winter  
208 and summer have revealed several details of the mean flow in the SCS: the large-scale  
209 circulation under the influence of northeasterly winter monsoon is stronger than that  
210 in the southwesterly summer monsoon, and the robust western boundary current in  
211 winter becomes relatively weak and unorganized in summer.

212

213 Eddies also have their own westward drift under the planetary  $\beta$  effect in the  
214 absence of any mean flow (Nof, 1981, Cushman-Roisin, 1994). Their propagation  
215 speed is approximately the phase speed of the first baroclinic Rossby waves with  
216 preferences for small poleward and equatorward deflection of cyclonic and  
217 anticyclonic eddies in the global ocean, respectively (Chelton et al., 2007).  
218 Theoretically, the phase speed of the first baroclinic Rossby wave is  $C_{R1} = -\beta R_1$ ,  
219 where the first baroclinic Rossby radius of deformation  $R_1$  is estimated using the  
220 climatological GDEM temperature and salinity data. Figure 2b (2e) shows the  
221 theoretical phase speed of nondispersive baroclinic Rossby waves calculated from  
222 GDEM winter (summer) climatological temperature and salinity data. The direction  
223 of the phase speed is due west and the magnitude increases from about 2 cm/s in the  
224 north latitude to 12 cm/s in the south latitude. It should be noted that the difference  
225 between the winter and summer distributions of the phase speed of the first baroclinic  
226 Rossby wave is relatively small. The underlying reason is that the variation of

227 seasonal stratification in the upper layer has little effect on the seasonal distribution of  
228 the first baroclinic Rossby deformation radius (Chelton et al, 1998, Cai et al., 2008).

229

230 The differences between the satellite observed propagation speed (Fig. 2a and 2d) and  
231 the propagation speed induced by the  $\beta$  effect (Fig. 2b and 2e) in winter and  
232 summer are shown in Fig. 2c and 2f, respectively, which may represent the  
233 propagation speed caused by the advection of mean flow. To further illustrate the  
234 advection effect of mean flow, the winter (summer) mean dynamic topography is  
235 superimposed on the propagation speed caused by the mean flow. As can be seen,  
236 there is a good spatial correlation (0.61 in the zonal direction and 0.52 in the  
237 meridional direction, both of which are significant at the 95% confidence level)  
238 between the cyclonic eddy propagation speed advected by the mean flow and the large  
239 scale surface cyclonic circulation in winter, both of which are centered northwest of  
240 the Luzon Island (Fig. 2c). Due to the weak cyclonic gyre in the NSCS, the spatial  
241 correspondence in summer is not as obvious as that in winter (Fig. 2f). Since the  
242 propagation speed induced by the  $\beta$  effect is westward, this tendency is reinforced  
243 by the mean flow in the north, but compensated by the mean flow in the south.  
244 Because the mean flow in the south is not so strong, it is not able to reverse eddy  
245 propagation from its westward motion induced by the  $\beta$  effect as in the Antarctic  
246 Circumpolar Current region (Klocker and Marshall, 2014) no matter in winter or  
247 summer.

248

249 To explore other possible causes of eddy propagation, Fig. 3a shows the annual mean  
250 eddy propagation speed. The most striking pattern is that the eddy propagation speed  
251 is accelerated markedly on the northern continental shelf of the NSCS (also can be  
252 seen in Fig. 2a and 2d), corresponding well to the region of negative maximum

253 meridional topographic  $\beta_r = \frac{f}{H} \frac{dH}{dy}$ , where  $H$  is the water depth. Their correlation  
254 is -0.40, which is significant at the 95% confidence level. This relatively good  
255 correspondence suggests that besides the planetary  $\beta$  effect and advection of mean  
256 flow, the topographic  $\beta$  effect also contributes to the eddy propagation in some  
257 regions where the bathymetry gradient cannot be neglected.

### 258 **3.2 Choice of Predictors**

259 As mentioned above, the mean flow advection and the effects of  $\beta$  (both planetary  
260 and topographic) are closely related with the eddy propagation. These factors should  
261 be considered as the potential predictors, and the seasonal climatological eddy zonal  
262 and meridional motions (U\_CLIM V\_CLIM) derived from the MCC are calculated to  
263 represent the effects of  $\beta$  and the mean flow advection. It is noted that we have tried  
264 to decompose U\_CLIM and V\_CLIM into the effects of  $\beta$  and the mean flow  
265 advection and incorporate them into the regression model, but found no improvement  
266 of the forecast skill.

267

268 In reality, the large-scale circulation evolves during the forecast period, this synoptic  
269 effect of mean flow advection should also be taken into account. To help account for  
270 the time variation of the mean flow advection, the current zonal and meridional  
271 absolute geostrophic flows (U\_ADT, V\_ADT) derived from the satellite data are  
272 evaluated at the beginning of the forecast time along the eddy trajectory. Besides, the  
273 persistence factors should also be considered in the regression model, since they  
274 contain the “latest” pattern of eddy propagation under the effects of  $\beta$  and the mean  
275 flow advection. The chosen persistence factors are the initial eddy position (LON,  
276 LAT) and the eddy motion past 1-week (U\_PAST, V\_PAST). All the chosen eight  
277 predictors are listed in Table 2, and can be derived along the eddy trajectories. They  
278 can be divided into two categories: 1) P1-P6 related to climatology and persistence,

279 i.e., “static predictors”, and 2) P7-P8 related to the changing environmental conditions,  
280 i.e., “synoptic predictors”.

281

282 The relative contribution of each predictor on each forecast period is illustrated by the  
283 normalized regression coefficient (Table 3). The larger the normalized regression  
284 coefficient, the greater its contribution to the individual forecast equation. Persistence  
285 factors (U\_PAST, V\_PAST) are initially the most important predictors, while after 2  
286 weeks the most important predictors are the climatology factors (U\_CLIM, V\_CLIM).  
287 The synoptic predictors (U\_ADT, V\_ADT) contribute less to the forecast equations  
288 comparing with persistence and climatology. The underlying reason may be that the  
289 week to week variations are too large so the representation of the initial U\_ADT and  
290 V\_ADT to the actual velocities in the 4-week window is not as good as the U\_CLIM  
291 and V\_CLIM.

## 292 **4. Performance of the Multiple Regression Model**

### 293 **4.1 Comparison with the persistence method**

294 To evaluate the performance of our prediction model, the persistence method and our  
295 model are used to predict the eddy trajectories during 2009-2013. The persistence  
296 method is a benchmark comparison and reference forecast widely accepted in the  
297 atmospheric and oceanic sciences (Mittermaier, 2008; Müller et al., 2012), which is  
298 defined as  $\chi_{t+1} = \chi_t$ , where  $\chi$  is any parameter, and t is a distance time step. In this  
299 study,  $\chi$  refers to the eddy propagation speed and the persistence means no change  
300 of propagation speed from the initial state (Fig. 4a). The root-mean-square error  
301 (RMSE) and correlation coefficient between the predicted and actual longitudes  
302 (latitudes), and mean distance errors of our model and persistence method over a  
303 4-week horizon are computed.

304

305 Table 4 lists the comparison of prediction results. It shows that our multiple linear

306 regression model beats the persistence method and indicates our model has some  
307 forecast skill (Table 5): the RMSE between the predicted and the actual longitudes  
308 (latitudes) throughout the 4-week horizon is 32.7-89.2 km (29.5-73.5 km) with the  
309 correlation coefficients  $>0.93$  ( $>0.95$ ).

310

311 As an example, Fig. 5 compares the 1-2 weeks forecast performances of our model  
312 (blue) and the persistence method (green) with the observation (red). Generally, the  
313 eddy trajectory predicted 1-2 weeks in advance by our model coincides well with the  
314 observed trajectory with an overall average error of 27.6 km (week-1) and 42.5 km  
315 (week-2), and even the convoluted pattern can be reproduced properly (Fig. 5 (right))  
316 though the mean error is slightly larger than the smooth case. In contrast, although the  
317 persistence forecast trajectory at week-1 is relatively consistent with the observation  
318 (Fig. 5a and 5b), the persistence method cannot forecast the eddy trajectories properly  
319 when the forecast horizon increases (Fig. 5c and 5d). To further compare their  
320 differences, their forecast distance errors are normalized with the Rossby radius on  
321 each forecast grid over 4-week forecast window, respectively. The correlation  
322 between the normalized forecast distance errors of the persistence method and our  
323 model decreases from 0.67 at week-1 to 0.38 at week-4. This is consistent with the  
324 above judgement and confirms the superiority of our multiple linear regression model  
325 over the persistence method.

## 326 **4.2 Sensitive Performance of Different Eddy Polarity and Season**

327 Previous studies have shown that anticyclonic eddies and cyclonic eddies in the NSCS  
328 have different dynamic characteristics, such as generation sites, rotation speeds and  
329 propagation trajectories, and the seasonal variability of these eddies is robust (Wang et  
330 al., 2006; Wang et al., 2008; Li et al., 2011). Two natural questions arise: 1) is there  
331 any difference on the model forecast ability between anticyclonic eddies (Fig. 1a) and  
332 cyclonic eddies (Fig. 1b)? 2) If so, is there any difference on the forecast ability for

333 one type of eddies in winter (Fig. 7a and 8a) and summer (Fig. 7b and 8b)? This  
334 section will explore the different model performances on two types of eddies and  
335 during different seasons in the NSCS.

336

337 The period considered for regressing and predicting the anticyclonic eddy and  
338 cyclonic eddy positions is the same as that used in developing the predictive model in  
339 Section 2.3. The mean forecast errors of anticyclonic (cyclonic) eddies from week-1  
340 to week-4 are 36.9 km (41.1 km), 62.6 km (68.1 km), 81.0 km (88.5 km), and 102.0  
341 km (108.2 km), respectively (Fig. 6). These results show that the forecast errors of  
342 anticyclonic eddies are smaller than those of cyclonic eddies in all forecast horizon,  
343 and the maximum error difference can reach 7.5 km at week-3. To investigate the  
344 underlying reasons of different model performances for anticyclonic eddies and  
345 cyclonic eddies, we use the persistence error ( $CC' = \sqrt{AB^2 + BC^2 - 2AB \cdot BC \cdot \cos \theta}$  in  
346 Fig. 4a) at week-1 as an index to measure the difficulty of trajectory forecast. The  
347 underlying reason in physics is that  $CC'$ , which includes the effects of winding angle  
348 ( $\theta$ , measuring the trajectory curvature) and the eddy propagation distances in the  
349 former and latter periods (AB and BC, measuring the eddy propagation speed), is an  
350 integral characteristic of eddy trajectory. The correlation between this integrated index  
351 and eddy trajectory forecast error is relatively high with  $R=0.62$  (Fig. 4b), which is  
352 significant at the 95% confidence level and shows its ability of measuring the inherent  
353 difficulty of trajectory forecast: the larger the index, the more difficult the trajectory  
354 forecast, thus the larger the forecast error. Because the indices (mean persistence  
355 errors) of all the anticyclonic and cyclonic eddy trajectories in the NSCS are 46.6 km  
356 and 53.0 km, respectively, it is not difficult to understand why the mean forecast error  
357 of anticyclonic eddy trajectories is smaller than that of cyclonic eddy trajectories in  
358 the NSCS. The index difference between anticyclonic and cyclonic eddy trajectories  
359 is caused by these different trajectory patterns (Fig. 1a and 1b), which could be due to  
360 the opposing meridional drifts of anticyclonic and cyclonic eddies expected from the  
361 combination of  $\beta$  effect and self-advection (Morrow et al., 2004).

362

363 Figure 7c (Fig. 8c) shows the mean forecast errors of anticyclonic (cyclonic) eddy  
364 trajectories in winter and summer over a 4-week horizon. Because the mean  
365 persistence error (42.0 km) of anticyclonic eddy trajectories in winter is smaller than  
366 that (51.9 km) in summer, as expected, the mean forecast error of anticyclonic eddy  
367 trajectories in winter is smaller than that in summer for all cases. This is also the case  
368 for the cyclonic eddy: since the mean persistence error (54.6 km) of cyclonic eddy  
369 trajectories in winter is relatively larger than that (52.8 km) in summer, the mean  
370 forecast error of cyclonic eddy trajectories in winter is larger than that in summer. The  
371 index difference of one type of eddy trajectories between winter and summer is also  
372 caused by the different trajectory patterns. Why do the anticyclonic and cyclonic  
373 eddies follow different trajectories in winter (Fig. 7a and 8a) and summer (Fig. 7b and  
374 7b)? One possible dynamical reason is the different interactions between the eddies  
375 and seasonal mean flows. Other underlying factors such as eddy generation  
376 mechanisms and eddy-topography interactions in different seasons may also  
377 contribute. This is beyond the scope of this study and needs further investigation  
378 using numerical models.

## 379 **5. Summary and Discussion**

380 In this study, we have investigated the underlying dynamics of the eddy propagation  
381 in the NSCS and found their propagation is mainly driven by the combination of the  
382 planetary  $\beta$  effect and mean flow advection. In addition, the topographic  $\beta$  effect  
383 also has some contribution to the eddy propagation where the bathymetry gradient  
384 cannot be neglected, like the steep continental shelf in the NSCS (Fig. 1a).

385

386 Based on the dynamical analysis, predictors are chosen and a simple statistical  
387 predictive model for relating various oceanic parameters to eddy propagation position  
388 changes is developed using the multiple linear regression method. This predictive  
389 model is made up of eight predictands (zonal and meridional displacements over 1-4

390 weeks) and eight predictors (six static predictors, two synoptic predictors). The six  
391 static predictors are associated with the initial position, the zonal and meridional  
392 motions past 1-week, and the climatological eddy zonal and meridional motions. The  
393 other two synoptic predictors account for the time variation of the mean flow  
394 advection. Results showed that this simple model has significant forecast skills over a  
395 4-week forecast horizon comparing the traditional persistence method. Moreover, the  
396 model performance is sensitive to eddy type and forecast season: 1) the predicted  
397 trajectory errors of anticyclonic eddies are smaller than those of cyclonic eddies; 2)  
398 the predicted trajectory errors of anticyclonic eddies in winter are smaller than those  
399 in summer; while the contrary is the case for the cyclonic eddy. The predictive model  
400 performance strongly depends on the inherent difficulty of trajectory forecast.

401

402 Although the performance of the proposed predictive model is encouraging, it could  
403 be refined further. Further improvement may be possible by including the effect of  
404 eddy-eddy interactions on the eddy propagation, which is supposed to help induce the  
405 eddy trajectory curve or loop (Early et al., 2011). Another possible improvement is to  
406 use artificial neural network (ANN) in developing the forecast model. ANN has been  
407 successfully used in the predicting cyclone tracks (Ali et al., 2007) and loop current  
408 variation (Zeng et al., 2015). ANN can represent both linear and non-linear  
409 relationships learned directly from the data being modeled. It mainly contains three  
410 layers: the input layer, the hidden layer, and the output layer. To be consistent with the  
411 multiple linear regression model, both the input layer and the output layer include the  
412 same predictors and predictands as the regression model, respectively. The hidden  
413 layer consists of two layers of neural variables. Through iterations on backward  
414 propagation of the error, the neural network learns by itself to achieve an optimum  
415 weighting function and a minimum error. The forecast errors of ANN for 1-4 weeks  
416 are listed in Table 4. We can see that some improvements (0.3-4.2 km during 1-4



417 weeks forecast horizon) have been shown comparing with the linear regression  
418 method. Recently, Jiang et al. (2018) have found the deep learning algorithm of neural  
419 networks performs better than the simple ANN for the parameterization of  
420 typhoon-ocean feedback in typhoon forecast models. These enhancements (both  
421 physics and algorithms) are topics warranting future research and development.

422

423 *Data availability.* The SLA and MDT data can be downloaded from AVISO  
424 (<ftp://ftp.aviso.oceanobs.com/>), and the NSCS eddy trajectory data can be derived  
425 from the 3rd release global eddy dataset (<http://cioss.coas.oregonstate.edu/eddies/>).

426

427 *Acknowledgements.* This work is supported by the National Key Research and  
428 Development Program of China (2017YFC1404103), the National Basic Research  
429 Program of China (2013CB430301), the Natural Science Foundation of China  
430 (91428206, 41621064, 91528304), the National Programme on Global Change and  
431 Air-Sea Interaction (GASIIPOVAI-04), and the China Postdoctoral Science  
432 Foundation (2016M601493).

433

## 434 **References**

435 Aberson, S. D. and Sampson, C. R.: On the predictability of tropical cyclone tracks in the  
436 northwest pacific basin, *Mon. Wea. Rev.*, 131, 1491-1497, 2003.

437 Ali, M. M., Kishtawal, C. M., and Jain, S.: Predicting cyclone tracks in the north Indian Ocean:  
438 An artificial neural network approach, *Geophys. Res. Lett.*, 34, L04603,  
439 <http://doi.org/10.1029/2006GL028353>, 2007.

440 Bao, S., Zhang, R. Wang, H., Yan, H., and Yu, Y.: Salinity profile estimation in the Pacific Ocean  
441 from satellite Surface salinity observations, *J. Atmos. Oceanic. Technol.*, 36, 53-68, 2019.

442 Cai, S., Long, X., Wu, R., and Wang, S.: Geographical and monthly variability of the first  
443 baroclinic rossby radius of deformation in the south china sea, *J. Mar. Syst.*, 74, 711-720, 2008.

444 Canes, M. R.: Description and evaluation of GDEM-V3.0, Rep.NRL/MR/7330-09-9165, Nav. Res.

445 Lab, Washington, D. C, 2009.

446 Chelton, D. B., Schlax, M. G., and Samelson, R. M.: Global observations of nonlinear mesoscale  
447 eddies, *Prog. Oceanogr.*, 91, 167-216, 2011.

448 Chelton, D. B., Schlax, M. G., Samelson, R. M., and de Szoeke, R. A.: Global observations of  
449 large oceanic eddies, *Geophys. Res. Lett.*, 34, L15606, <http://doi.org/10.1029/2007GL030812>,  
450 2007.

451 Chelton, D., DeSzoeke, R., and Schlax, M.: Geographical variability of the first baroclinic rossby  
452 radius of deformation, *J. Phys. Oceanogr.*, 28, 433-460, 1998.

453 Chen, G., Hou, Y., and Chu, X.: Mesoscale eddies in the South China Sea: Mean properties,  
454 spatiotemporal variability, and impact on thermohaline structure, *J. Geophys. Res.*, 116, C06018,  
455 <http://doi.org/10.1029/2010JC006716>, 2011.

456 Cushman-Roisin, B.: *Introduction to Geophysical Fluid Dynamics*, Prentice Hall, 320 pp, 1994.

457 Demaria, M. and Kaplan, J.: A statistical hurricane intensity prediction scheme (SHIPS) for the  
458 Atlantic basin, *Weather Forecast*, 9, 209-220, 1994.

459 Dominiak, S., and Terray, P.: Improvement of ENSO prediction using a linear regression model  
460 with a southern Indian Ocean sea surface temperature predictor, *Geophys. Res. Lett.*, 32,  
461 L18702, [doi:10.1029/2005GL023153](http://doi.org/10.1029/2005GL023153), 2005.

462 Dong, C., McWilliams, J. C., Liu, Y., and Chen, D.: Global heat and salt transports by eddy  
463 movement, *Nature Communications*, 5, 3294, 2014.

464 Ducet, N., Le Traon, P. Y., and Reverdin, G.: Global high-resolution mapping of ocean circulation  
465 from TOPEX/Poseidon and ERS-1 and -2, *J. Geophys. Res.*, 105, 19477–19498,  
466 <http://doi.org/10.1029/2000JC900063>, 2000.

467 Early, J. J., Samelson, R. M., and Chelton, D. B.: The evolution and propagation of  
468 quasigeostrophic ocean eddies, *J. Phys. Oceanogr.*, 41, 1535-1555, 2011.

469 Emery, W. J., Thomas, A. C., Collins, M. J., Crawford, W. R., and Mackas, D. L.: An objective  
470 method for computing advective surface velocities from sequential infrared satellite images, *J.*  
471 *Geophys. Res.*, 91, 12865–12878, <http://doi.org/10.1029/JC091iC11p12865>, 1986.

472 Fu, L.-L.: Pathways of eddies in the South Atlantic Ocean revealed from satellite altimeter  
473 observations, *Geophys. Res. Lett.*, 33, L14610, <http://doi.org/10.1029/2006GL026245>, 2006.

474 Fu, L.-L.: Pattern and speed of propagation of the global ocean eddy variability, *J. Geophys.*

475 Res., 114, C11017, <http://doi.org/10.1029/2009JC005349>, 2009.

476 Hurlburt, H., Chassignet, E., Cummings, J., Kara, A., Metzger, E., Shriver, J., Smedstad, O.,  
477 Wallcraft, A., and Barron, C.: Eddy Resolving Global Ocean Prediction, Washington D. C.,  
478 American Geophysical Union Geophysical Monograph Series, 353-381, 10.1029/177GM21,  
479 2008.

480 Jiang, G-Q., Xu, J., & Wei, J.: A deep learning algorithm of neural network for the  
481 parameterization of typhoon-ocean feedback in typhoon forecast models, *Geophys. Res. Lett.*,  
482 45, <https://doi.org/10.1002/2018GL077004>, 2018.

483 Klocker, A. and Marshall, D. P.: Advection of baroclinic eddies by depth mean flow, *Geophys. Res.*  
484 *Lett.*, 41, 3517–3521, <http://doi.org/10.1002/2014GL060001>, 2014.

485 Leese, J. A., Novak, C. S., and Clark, B. B.: An automated technique for obtaining cloud motion  
486 from geosynchronous satellite data using cross correlation, *J. Appl. Meteor.*, 10, 18-132, 1971.

487 Li, J., Zhang, R., and Jin, B.: Eddy characteristics in the northern South China Sea as inferred  
488 from Lagrangian drifter data, *Ocean Sci.*, 7, 1575-1599, 2011.

489 Li, J., Wang, G., and Zhai, X.: Observed cold filaments associated with mesoscale eddies in the  
490 South China Sea, *J. Geophys. Res. Oceans*, 122, 762–770,  
491 <http://doi.org/10.1002/2016JC012353>, 2017.

492 Liu, W. T. and Xie, X.: Space-based observations of the seasonal changes of South Asian  
493 monsoons and oceanic response, *Geophys. Res. Lett.*, 26, 1473-1476, 1999.

494 Ma, X. and Coauthors: Western boundary currents regulated by interaction between ocean eddies  
495 and the atmosphere, *Nature*, 535, 533, 2016.

496 Matear, R. J., and McNeil, B. I.: Decadal accumulation of anthropogenic CO<sub>2</sub> in the Southern  
497 Ocean: A comparison of CFC-age derived estimates to multiple-linear regression estimates,  
498 *Global Biogeochem. Cycles*, 17(4), 1113, doi:10.1029/2003GB002089, 2003.

499 Morrow, R., Birol, F., Griffin, D., and Sudre, J.: Divergent pathways of cyclonic and anti-cyclonic  
500 ocean eddies, *Geophys. Res. Lett.*, 31, L24311, <http://doi.org/10.1029/2004GL020974>, 2004.

501 Mittermaier, M.: The potential impact of using persistence as a reference forecast on perceived  
502 forecast skill, *Weather Forecast*, 23, 1022-1031, 2008.

503 Müller, W. A., Baehr, J., Haak, H., Jungclaus, J. H., Kröger, J., Matei, D., Notz, D., Pohlmann, H.,  
504 von Storch, J. S., and Marotzke, J.: Forecast skill of multi-year seasonal means in the decadal

505 prediction system of the Max Planck Institute for Meteorology, *Geophys. Res. Lett.*, 39, L22707,  
506 <http://doi.org/10.1029/2012GL053326>, 2012.

507 Ninnis, R. M., Emery, W. J., and Collins, M. J.: Automated extraction of pack ice motion from  
508 advanced very high resolution radiometer imagery, *J. Geophys. Res.*, 91, 10725–10734,  
509 <http://doi.org/10.1029/JC091iC09p10725>, 1986.

510 Nof, D.: On the  $\beta$ -induced movement of isolated baroclinic eddies, *J. Phys. Oceanogr.*, 11,  
511 1662-1672, 1981.

512 Oey, L.-Y., Ezer, T., Forristall, G., Cooper, C., DiMarco, S., and Fan, S.: An exercise in forecasting  
513 loop current and eddy frontal positions in the Gulf of Mexico, *Geophys. Res. Lett.*, 32, L12611,  
514 <http://doi.org/10.1029/2005GL023253>, 2005.

515 Rienecker, M. M., Mooers, C. N. K., and Robinson, A. R.: Dynamical interpolation and forecast of  
516 the evolution of mesoscale features off northern California, *J. Phys. Oceanogr.*, 17, 1189-1213,  
517 1987.

518 Rio, M.-H. and Hernandez, F.: A mean dynamic topography computed over the world ocean from  
519 altimetry, in situ measurements, and a geoid model, *J. Geophys. Res.*, 109, C12032,  
520 <http://doi.org/10.1029/2003JC002226>, 2004.

521 Robinson, A. R., Carton, J. A., Mooers, C. N. K., Walstad, L. J., Carter, E. F., Rienecker, M. M.,  
522 Smith, J. A., and Leslie, W. G.: A real-time dynamical forecast of ocean synoptic/mesoscale  
523 eddies, *Nature*, 309, 781-783, 1984.

524 Seo, K. H., Wang, W., Gottschalck, J., Zhang, Q., Schemm, J.-K., Higgins, W., and Kumar, A.:  
525 Evaluation of MJO Forecast Skill from Several Statistical and Dynamical Forecast Models, *J*  
526 *Clim.*, 22(9), 2372-2388, 2009.

527 Shaw, P. T.: Seasonal variation of the intrusion of the Philippine Sea water into the South China  
528 Sea, *J. Geophys. Res.*, 96, 821-827, 1991.

529 Wang, G., Chen, D., and Su, J.: Generation and life cycle of the dipole in the South China Sea  
530 summer circulation, *J. Geophys. Res.*, 111, C06002, <http://doi.org/10.1029/2005JC003314>,  
531 2006.

532 Wang, G., Chen, D., and Su, J.: Winter eddy genesis in the eastern South China Sea due to  
533 orographic wind-jets, *J. Phys. Oceanogr.*, 38, 726–732, <http://doi.org/10.1175/2007JPO3868.1>,  
534 2008.

535 Wang, G., Li, J., Wang, C., and Yan, Y.: Interactions among the winter monsoon, ocean eddy and  
536 ocean thermal front in the South China Sea, *J. Geophys. Res.*, 117, C08002,  
537 <http://doi.org/10.1029/2012JC008007>, 2012.

538 Wang, G., Su, J., and Chu, P. C.: Mesoscale eddies in the South China Sea observed with altimeter  
539 data, *Geophys. Res. Lett.*, 30, 2121, <http://doi.org/10.1029/2003GL018532>, 21, 2003.

540 Xiu, P., Chai F., Shi, L., Xue, H., and Chao, Y.: A census of eddy activities in the South China Sea  
541 during 1993–2007, *J. Geophys. Res.*, 115, C03012, <http://doi.org/10.1029/2009JC005657>, 2010.

542 Zhang, R.: Mechanisms for the low frequency of summer Arctic sea ice extent, *Proc. Natl. Acad.*  
543 *Sci.*, 112(15), 4570-4575, 2015.

544 Zhang, Z., Wang, W., and Qiu, B.: Oceanic mass transport by mesoscale eddies, *Science*, 345, 322,  
545 2014.

546 Zeng, X., Li, Y., and He, R.: Predictability of the loop current variation and eddy shedding process  
547 in the Gulf of Mexico using an artificial neural network approach, *J. Atmos. Oceanic. Technol.*,  
548 32, 1098-1111, 2015.

549 Zhuang W., Du, Y., Wang, D., Xie, Q., and Xie, S.-P.: Pathways of mesoscale variability in the  
550 South China Sea, *Chin. J. Oceanol. Limnol.*, 28, 1055-1067, 2010.

551

552

553 **Figure and Table Captions**

554 **Figure 1.** The trajectories of (a) anticyclonic and (b) cyclonic eddies with lifetime  $\geq 5$   
555 weeks in the northern South China Sea (SCS). The solid circle represents the ending  
556 position of each trajectory. In Fig. 1a, TI: Taiwan Island, LI: Luzon Islands, VN:  
557 Vietnam. The two isobaths are for 200 m and 2000 m, respectively.

558 **Figure 2.** Winter climatology of (a) eddy propagation speed directions (vectors) and  
559 magnitudes (color, cm/s), (b) The phase speed directions (vectors) and magnitudes  
560 (color, cm/s) of the first baroclinic Rossby wave. (c) The speed difference (vectors)  
561 between (a) and (b) superimposed on the winter mean absolute dynamic topography  
562 (color, cm). (d), (e) and (f) are the same as (a), (b) and (c), respectively, but for the  
563 summer.

564 **Figure 3.** (a) Annual mean of eddy propagation speed directions (vectors) and  
565 magnitudes (color, cm/s). (b) Meridional distribution of the topographic  $\beta$  effect  
566 (color shading).

567 **Figure 4.** (a) Schematic of persistence method. A, B, and C are three observed eddy  
568 positions on the trajectory every 1 week interval. C' is the predictive eddy position 1  
569 week in advance by persistence method, that is  $BC'=AB$ . Thus  $CC'$  is the persistence  
570 error at week-1. (b) Scatterplot of persistence error versus forecast error of our model  
571 at week-1 with best fit linear regression.

572 **Figure 5.** A comparison of the satellite observed trajectory (red), the predicted  
573 trajectory by our model (blue) and persistence trajectory (green) at (a) week-1, (c)  
574 week-2. (b), (d) are the same as (a) and (c), respectively, but for a recurved trajectory.  
575 The biweekly eddy positions on each trajectory are shown by the solid circles. The  
576 ending position of each trajectory is represented by the solid triangle.

577

578 **Figure 6.** Comparison of the mean forecast errors between anticyclonic eddies (red)  
579 and cyclonic eddies (blue) over a 4-week window.

580 **Figure 7.** The trajectories of anticyclonic eddies in (a) winter and (b) summer with  
581 lifetime  $\geq 5$  weeks in the northern South China Sea. The solid circle represents the  
582 ending position of each trajectory. (c) Comparison of their mean forecast errors over a  
583 4-week window.

584 **Figure 8.** The same as Fig. 6, but for the cyclonic eddies.

585

586 **Table 1.** The eight predictands used in the predictive model.

587 **Table 2.** The eight predictors used in the predictive model.

588 **Table 3.** Normalized regression coefficients  $a_{i,j}$  ( $b_{i,j}$ ) for use with the eddy zonal  
589 (meridional) motion prediction equation.

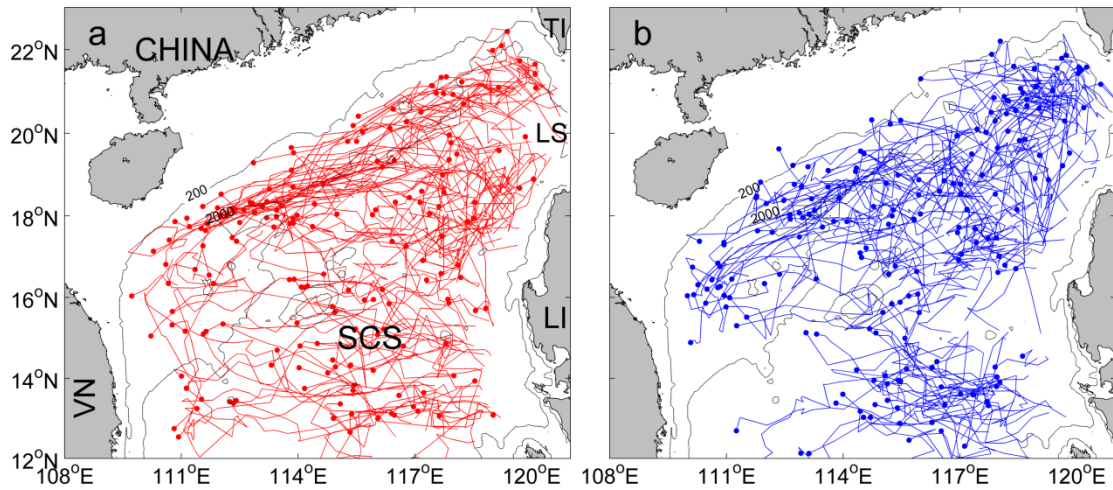
590 **Table 4.** Comparison of mean forecast distance errors (km) of the persistence,  
591 multiple linear regression (MLR), and artificial neural network (ANN) method.

592 **Table 5.** Statistics of our multiple linear regression model for different forecast time of  
593 eddy propagation positions in terms of longitudes (latitudes).

594

595

596



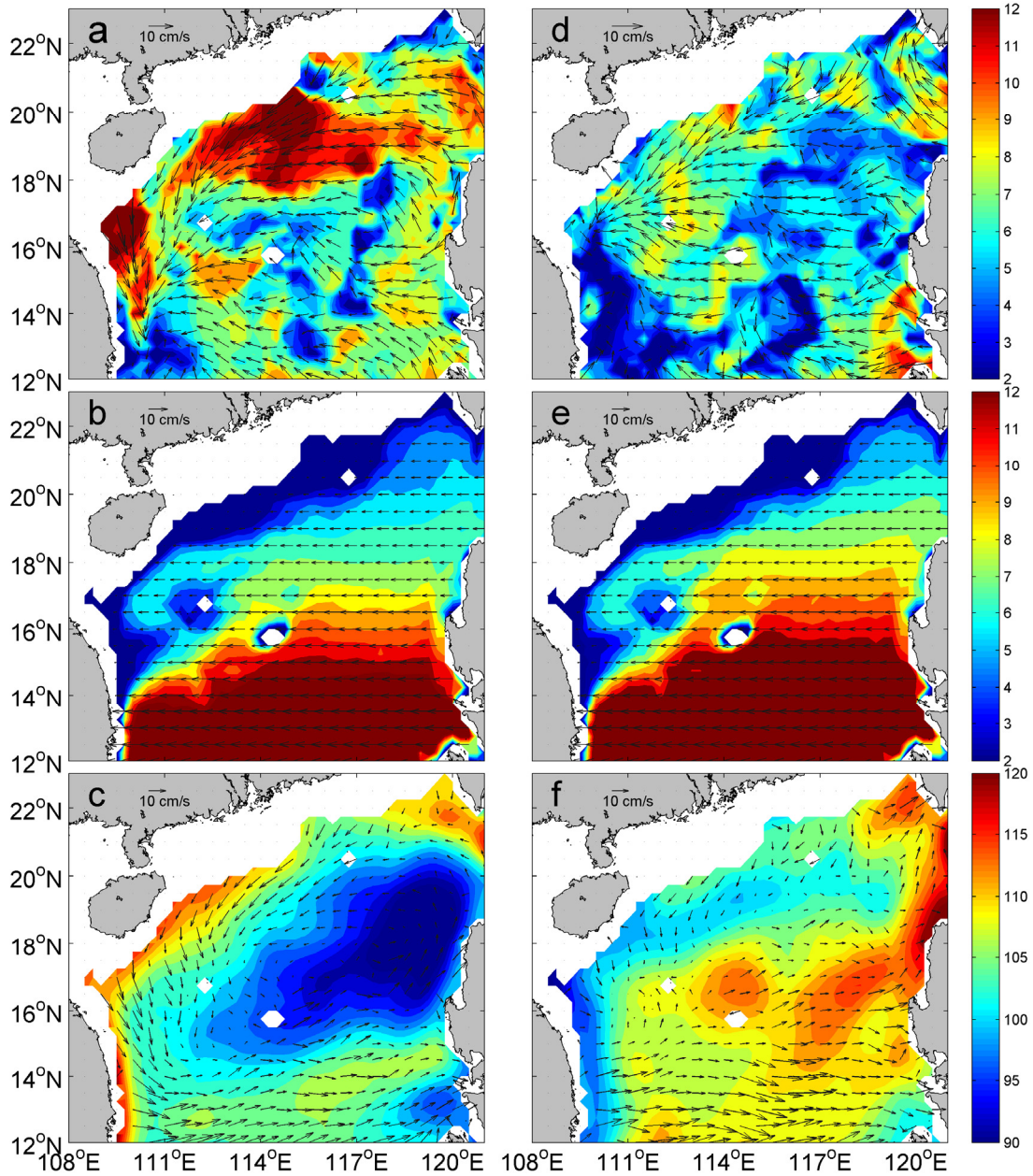
597

598

599 **Figure 1.** The trajectories of (a) anticyclonic and (b) cyclonic eddies with lifetime  $\geq 5$   
600 weeks in the northern South China Sea (SCS). The solid circle represents the ending  
601 position of each trajectory. In Fig. 1a, TI: Taiwan Island, LI: Luzon Islands, VN:  
602 Vietnam. The two isobaths are for 200 m and 2000 m, respectively.

603



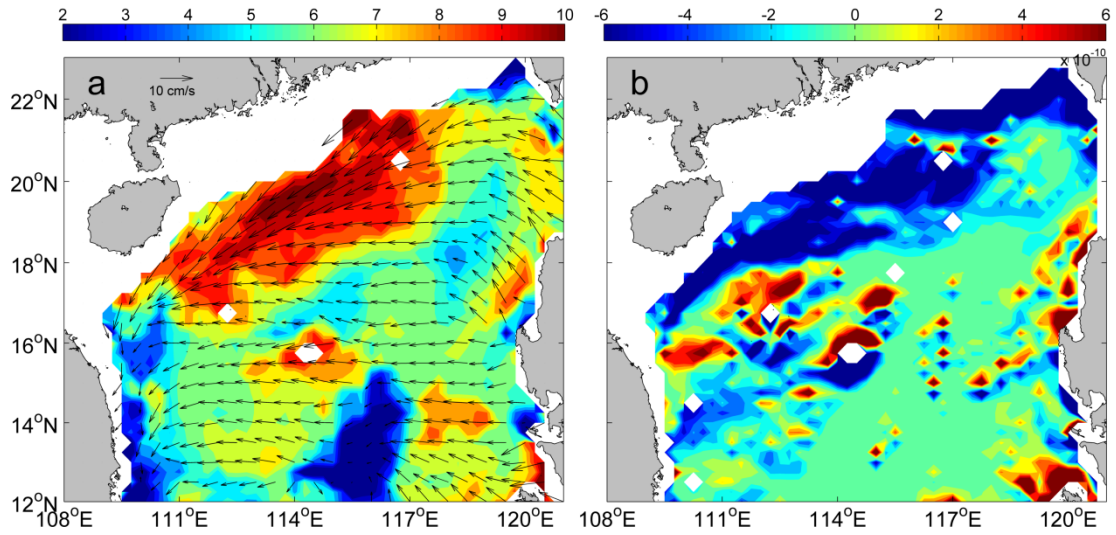


604

605

606 **Figure 2.** Winter climatology of (a) eddy propagation speed directions (vectors) and  
 607 magnitudes (color, cm/s), (b) The phase speed directions (vectors) and magnitudes  
 608 (color, cm/s) of the first baroclinic Rossby wave. (c) The speed difference (vectors)  
 609 between (a) and (b) superimposed on the winter mean absolute dynamic topography  
 610 (color, cm). (d), (e) and (f) are the same as (a), (b) and (c), respectively, but for the  
 611 summer.

612



613

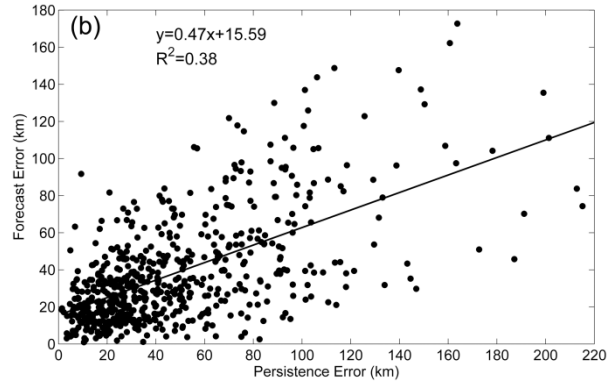
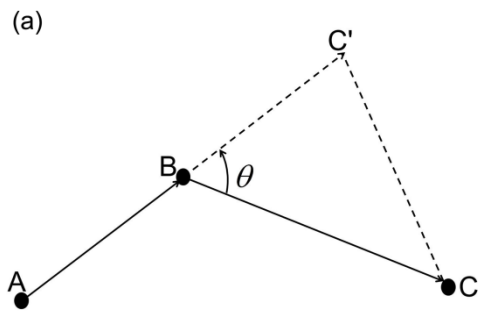
614

615 **Figure 3.** (a) Annual mean of eddy propagation speed directions (vectors) and

616 magnitudes (color, cm/s). (b) Meridional distribution of the topographic  $\beta$  effect

617 (color shading).

618

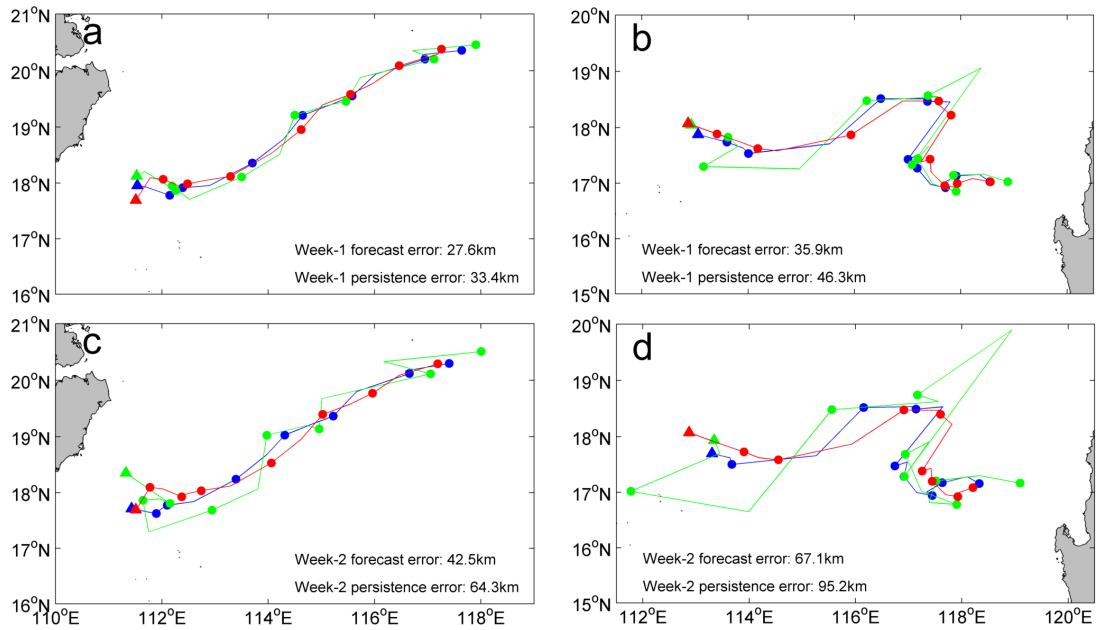


619

620

621 **Figure 4.** (a) Schematic of persistence method. A, B, and C are three observed eddy  
 622 positions on the trajectory every 1 week interval. C' is the predictive eddy position 1  
 623 week in advance by persistence method, that is  $BC'=AB$ . Thus  $CC'$  is the persistence  
 624 error at week-1. (b) Scatterplot of persistence error versus forecast error of our model  
 625 at week-1 with best fit linear regression.

626



627

628

629 **Figure 5.** A comparison of the satellite observed trajectory (red), the predicted

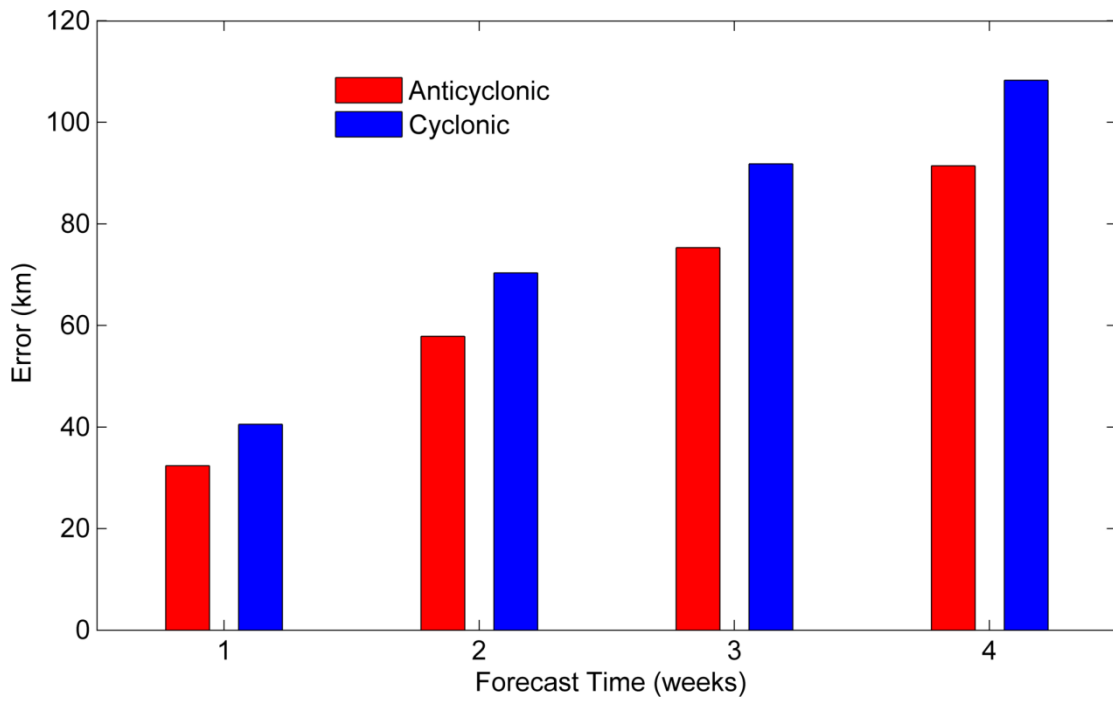
630 trajectory by our model (blue) and persistence trajectory (green) at (a) week-1, (c)

631 week-2. (b), (d) are the same as (a) and (c), respectively, but for a recurved trajectory.

632 The biweekly eddy positions on each trajectory are shown by the solid circles. The

633 ending position of each trajectory is represented by the solid triangle.

634

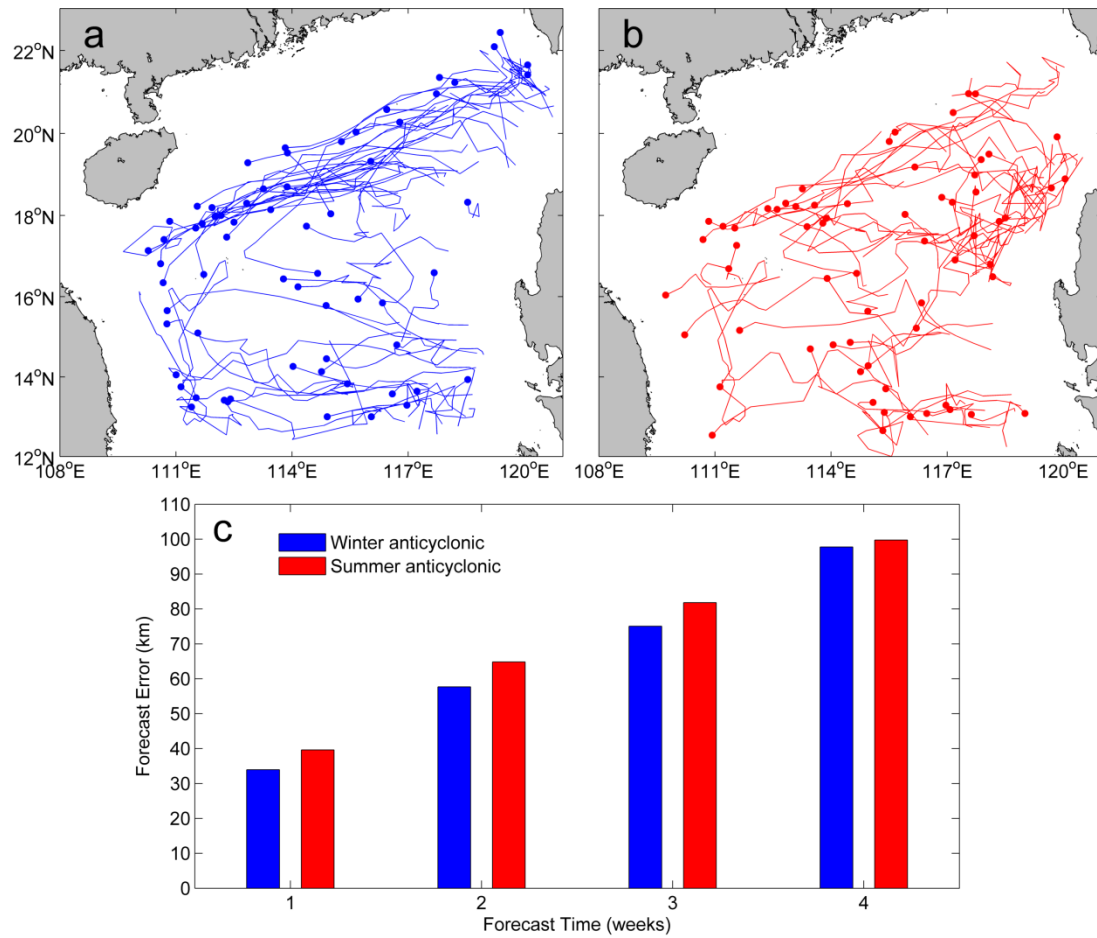


635

636 **Figure 6.** Comparison of the mean forecast errors between anticyclonic eddies (red)  
637 and cyclonic eddies (blue) over a 4-week window.

638

639



640

641

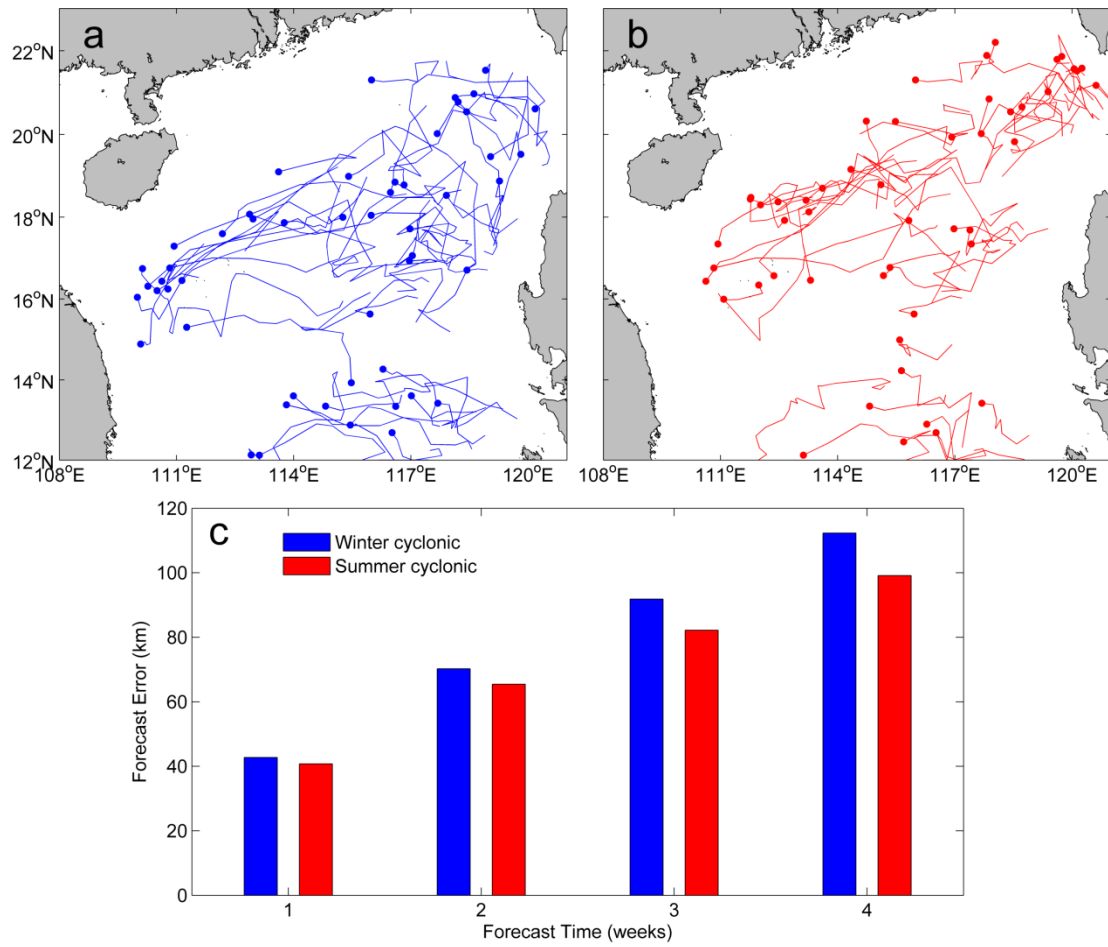
642 **Figure 7.** The trajectories of anticyclonic eddies in (a) winter and (b) summer with

643 lifetime  $\geq 5$  weeks in the northern South China Sea. The solid circle represents the

644 ending position of each trajectory. (c) Comparison of their mean forecast errors over a

645 4-week window.

646



647  
 648  
 649  
 650  
 651

**Figure 8.** The same as Fig. 6, but for the cyclonic eddies.

652 **Table 1.** The eight predictands used in the predictive model

653

Predictand	Symbol
1-week zonal displacement	$DX_1$
1-week meridional displacement	$DY_1$
2-week zonal displacement	$DX_2$
2-week meridional displacement	$DY_2$
3-week zonal displacement	$DX_3$
3-week meridional displacement	$DY_3$
4-week zonal displacement	$DX_4$
4-week meridional displacement	$DY_4$

654

655



656 **Table 2.** The eight predictors used in the predictive model

657

Predictor	Symbol
Initial longitude (LON)	P <sub>1</sub>
Initial latitude (LAT)	P <sub>2</sub>
Eddy zonal motion past 1-week (U_PAST)	P <sub>3</sub>
Eddy meridional motion past 1-week (V_PAST)	P <sub>4</sub>
Climatological eddy zonal motion from MCC (U_CLIM)	P <sub>5</sub>
Climatological eddy meridional motion from MCC (V_CLIM)	P <sub>6</sub>
Initial zonal absolute geostrophic flow (U_ADT)	P <sub>7</sub>
Initial meridional absolute geostrophic flow (V_ADT)	P <sub>8</sub>

658

659 **Table 3.** Normalized regression coefficients  $a_{i,j}$  ( $b_{i,j}$ ) for use with the eddy zonal (meridional)  
 660 motion prediction equation

661

	j=1	j=2	j=3	j=4
i=1	-0.10 (0.03)	-0.14 (0.04)	-0.18 (0.05)	-0.24 (0.06)
i=2	0.10 (0.02)	0.13 (0.01)	0.16 (0.00)	0.18 (-0.03)
i=3	0.26 (0.00)	0.21 (0.03)	0.19 (0.07)	0.18 (0.09)
i=4	-0.02 (0.19)	-0.01 (0.10)	0.01 (0.08)	0.00 (0.08)
i=5	0.14 (0.09)	0.19 (0.13)	0.23 (0.16)	0.26 (0.16)
i=6	0.05 (0.17)	0.07 (0.23)	0.09 (0.26)	0.16 (0.27)
i=7	-0.05 (0.02)	-0.07 (0.02)	-0.07 (0.02)	-0.07 (0.03)
i=8	-0.03 (-0.07)	-0.01 (-0.08)	0.02 (-0.09)	0.04 (-0.09)

662

663

664 **Table 4.** Comparison of mean forecast distance errors (km) of the persistence, multiple linear  
 665 regression (MLR), and artificial neural network (ANN) method  
 666

Forecast weeks	Persistence	MLR	ANN
1	47.6	38.1	37.8
2	95.2	64.8	64.1
3	135.0	86.6	84.7
4	180.5	106.5	102.3

667 **Table 5.** Statistics of our multiple linear regression model for different forecast time of eddy propagation positions in terms of longitudes (latitudes)  
 668

Forecast weeks	Total/Predicted Number of Points	RMSE, km	Correlation Coefficient	Mean Distance Error, km
1	2604/623	32.7 (29.5)	0.99 (0.99)	38.1
2	2310/549	55.1 (47.3)	0.97 (0.98)	64.8
3	2016/475	72.5 (61.4)	0.95 (0.97)	86.6
4	1722/401	89.2 (73.5)	0.93 (0.95)	106.5

669 Note: the total/predicted number of points refers to the eddy positions at 7-day time interval in the whole/predicted eddy trajectories during 1992-2013/2009-2013;  
 670 the RMSE is the root mean square error between the predicted and the observed longitude (latitude).

671